We are IntechOpen,
the world's leading publisher of Open Access books
Built by scientists, for scientists

6,900
Open access books available

186,000
International authors and editors

200M
Downloads

154
Countries delivered to

Our authors are among the

TOP 1%
most cited scientists

12.2%
Contributors from top 500 universities

BOOK CITATION INDEX
CLARIVATE ANALYTICS
INDEXED

WEB OF SCIENCE™

Selection of our books indexed in the Book Citation Index
in Web of Science™ Core Collection (BKCI)

Interested in publishing with us?
Contact book.department@intechopen.com

Numbers displayed above are based on latest data collected.
For more information visit www.intechopen.com

Application of Nanoindentation Technique in Martensitic Structures

L. Zhang, T. Ohmura and K. Tsuzaki

Additional information is available at the end of the chapter

http://dx.doi.org/10.5772/48327

1. Introduction

The instrumented nanoindentation technique with a capability of in situ scanning-probe microscopy (SPM) or atomic force microscopy (AFM) can measure the mechanical properties of a precise site in a microstructure with accuracy within a nanometer [1]. As a precise and quantitative measuring method, nanoindentation technique has been widely used in various materials systems. In this chapter, the application of nanoindentation technique in the martensitic structures (lath martensite [2, 3] and lenticular martensite [4] as illustrated in Fig. 1) will be introduced. Also, to understand the relationship between martensitic transformation with grain size, nanostructured NiTi shape memory alloy [5] with a graded surface nanostructure was produced by surface mechanical attrition treatment (SMAT) and tested by nanoindentation.
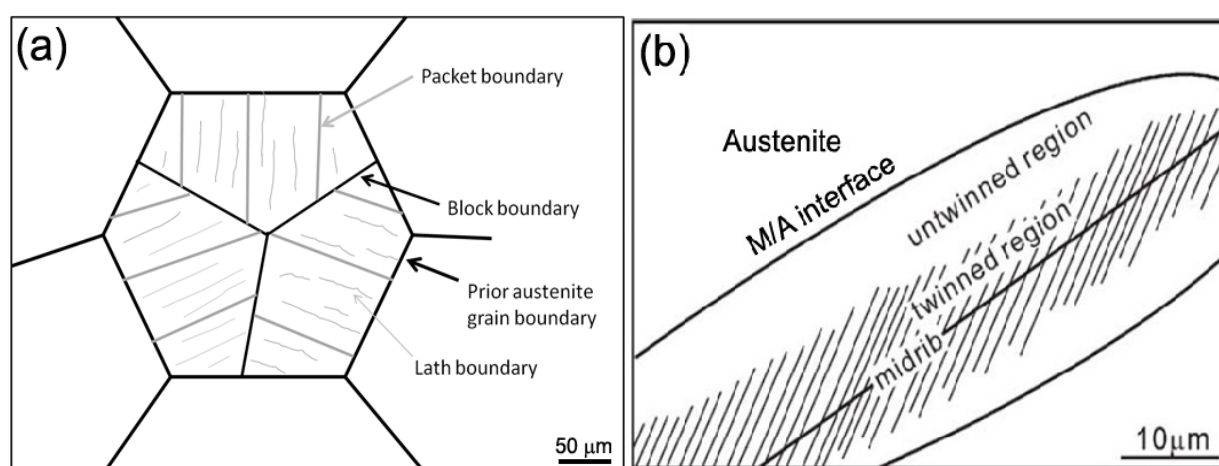

Figure 1. Schematic drawing of three packets of lath martensite within a prior austenite grain (a) and a lenticular martensite plate (b).

INTECH
open science | open minds

As one of the most important structural materials, the morphology and substructure of martensite in the Fe-Ni/Fe-C alloys have been investigated widely. The formation of various morphologies such as lath, butterfly, lenticular and thin plate has been shown to depend on the alloy composition or the transformation temperature (Ms Temperature). Each of them is unique in crystallographic features as well as in substructure [6]. Fig. 1 is schematic drawing of three packets of lath martensite within a prior austenite grain (a) and a lenticular martensite plate (b).

1.1. Lath martensite

Lath martensite, which forms in the highest temperature range, consists of parallel platelets or laths containing a high density of random dislocations [7, 8]. The lath martensite is mainly composed of four structural units: lath, block, packet and prior austenite grain (Fig. 1(a)). The prior austenite grain consists of some packets, the packet is divided into the blocks, and the block is subdivided into the lath structure. Only the lath boundaries are low-angle ones [9-12]. Hence the block structure can be recognized as an effective grain. Many studies have revealed that the macroscopic strength of the martensite in Fe-C-based alloys depends mainly on the carbon content [13] and tempering temperatures [14]. These dependences are understood as a matrix strengthening such as a carbon solid solution, dislocation interaction and fine precipitation strengthening. However, matrix strength (i.e. block matrix connecting solid solution, dislocation interaction and fine precipitation strengthening etc. of the matrix) without the contributions of high-angle boundaries has never been measured directly. Nanoindentation test with indent sizes much smaller than the block width is the key to obtain an exact measurement of the matrix strength without contributions of the high-angle boundaries, i.e. block boundaries. Simple alloy systems such as pure Fe-C binary alloy are suitable for conducting systematic investigations.

1.2. Lenticular martensite

On the other hand, lenticular martensite, which is plate-like with curved interfaces, forms at the intermediate temperature between lath martensite and thin plate martensite. The substructure of lenticular martensite is much more complicated than that of the other types. The martensite in the Fe-Ni alloy containing about 28.5% ~ 33 wt% Ni is lenticular with three regions, namely the mid-rib region, the twinned region and the untwined region [15]. The midrib region, where the martensitic transformation is thought to begin, has a substructure of fine transformation twins. The twin spacing is 6.9 nm in the Fe-31 wt% Ni alloy which was cooled just below the Ms temperature (223 K) [10, 16]. The twinned region is partially twinned, and the untwined region does not contain any twins but has many dislocations similar to that of the lath martensite [17, 18]. Since various lattice defects such as ultra-fine twins and dislocations exist simultaneously in one sample, the lenticular martensite in the Fe-Ni alloy is appropriate for understanding the strengthening mechanism in the structural materials.

As shown in Fig. 1, the microstructure of the martensite is complex and very fine on the submicron scale, so it is difficult to separate the strength contribution of each factor by the conventional macroscopic testing method. To understand the whole strengthening

mechanism of martensite, it is important to estimate each factor independently and reveal the relationship between the microstructure and the deformation behavior.

1.3. NiTi shape memory alloy

Nanoindentation technique can not only be used to characterize mechanical properties in transformed martensite, but also to detect the martensitic transformation during deformation. In NiTi alloys the reversible thermoelastic martensitic transformation can be induced by either temperature or stress and leads to their well-known shape memory and superelastic properties [19]. This thermoelastic martensitic transformation indicates a close, intrinsic interaction between microscopic phase transformations and macroscopic mechanical properties, resulting in complex mechanical behavior and uncertainty in determining the mechanical properties of NiTi. The stress-induced martensitic transformation (SIM) may contribute to the apparent elastic strain in the stress–strain test, leading to a low apparent Young's modulus [20, 21]. Despite suggestions by previous studies, direct evidence for the effect of the SIM on the Young's modulus is still lacking. Recent transmission electron microscopy (TEM) observations have indicated that the martensitic transformation is suppressed in nanocrystalline NiTi because of grain size effects [22]. In a very recent study [23] it was also suggested that a higher stress is required for the SIM for a smaller grain size. Therefore, it is important to investigate the effect of grain size on the Young's modulus in nanostructured NiTi. To understand the relationship between martensitic transformation with grain size, nanostructured NiTi with a graded surface nanostructure was produced by surface mechanical attrition treatment (SMAT).

2. Experimental procedures

2.1. Fe-C lath martensite and Fe-Ni lenticular martensite

Same experimental procedures were applied in Fe-C lath martensite and Fe-Ni lenticular martensite samples. The specimen surfaces for nanoindentation were mechanically polished with care, and subsequently electropolished. Nanoindentation measurements were carried out using a Hysitron, Inc. Triboscope with a Berkovich indenter. The tip truncation of the indenter was calibrated using fused silica. The Oliver and Pharr method [16] was used for the tip calibration and the calculation of nanohardness. The probed sites and the shape of the indent marks on the specimen surface were confirmed before and after the indentation measurements with the AFM mounted with the Triboscope. The conducted peak load was 500 µN. The loading/unloading rate was 50 µN/s and was held at the peak load for 10 s. Conventional Vickers hardness (H_v) tests as a macroscopic strength evaluation were conducted with a load of 4.9 N.

2.2. TiNi shape memory alloy

For nanoindentation the SMAT surface was protected with an electroplated Ni coating. Cross-sectional samples were carefully polished with decreasing grit sizes. The final polishing agent was a mixture of OP-S (0.04 µm colloid Si, Struers Inc.), H_2O_2 and NH_3-H_2O solutions (50:1:1) to reduce possible surface damage. After polishing, the state of the sample

surface was further confirmed by scanning electron microscopy and electron backscattering diffraction.

Nanoindentation measurements were carried out using a Hysitron, Inc. TriboIndenter with a Berkovich indenter. The tip truncation of the indenter was calibrated using fused silica. The Oliver and Pharr method [16] was used for the tip calibration and the calculation of nanohardness. The position and configuration of the indents were checked in situ by SPM. A peak load of 1000 µN was used with a loading/unloading rate of 50 µN/s and the indenter was held at peak load for 5 s before unloading.

The calculated modulus by an analysis of the unloading curve is reduced modulus E_r and its relationship with the Young's modulus is expressed as:

$$E_r^{-1} = \frac{1-\nu_s^2}{E_s} + \frac{1-\nu_i^2}{E_i},\tag{1}$$

where E_s and ν_s are the Young's modulus and the Poisson's ratio for the specimen, and E_i and ν_i are the same parameters for the indenter (1140 GPa and 0.07, respectively). Using 0.35 for the Poisson's ratio of NiTi [5], the value of E for NiTi can be determined.

3. Nanoindentation in Fe-C lath martensite

We firstly start with high purity Fe-C binary alloys which contain as-quenched lath martensite. Five nominal carbon contents of 0.1, 0.2, 0.4, 0.6 and 0.8 wt% (shorted as Fe-0.1C, 0.2C, 0.4C, 0.6C and 0.8C) were employed. A Fe-23wt% Ni alloy with lath martensite (shorted for Fe-23Ni) was also used for comparison.

3.1. Microstructures of Fe-C lath martensite

Fig. 2 represents the optical micrographs of the Fe-C lath martensite with different carbon content [2]. The block width deceases with increasing carbon content. The microstructure of the Fe-0.1C martensite composes clearly packets and blocks but for higher carbon content specimens, the block structure is very fine and complicated so it is hard to identify the boundaries of the block and packet. The microstructure of the Fe-23Ni lath martensite consists of blocks with a relatively large width typically in a few 10 µm.

3.2. Conventional nanoindentation in Fe-C lath martensite

Fig. 3 shows the typical load-displacement curves of five Fe-C martensites [2]. The smaller penetration depths show higher nanohardness values on the load-depth curve under the same peak load conditions. Maximum penetration depths of nanoindentation are less than 60 nm at the 500 µN peak load for all of the specimens. There is no indent size effect when the contact depth is in the range of 20 nm to 100 nm [24]. The previous study showed that the typical size of lath width is about 200 nm for carbon contents higher than 0.05 %. On the hemispherical approximation [25], the plastic zone sizes corresponding to the depths are estimated to be submicron in diameter, comparable to or

smaller than the typical block size because the martensite block consists of several laths with identical crystal orientation. Therefore, the measured nanohardness H_n can be considered to be dominated by the matrix strength. A grain boundary might exist just beneath the indenter or within the plastic zone in some cases. However, the number of the boundaries associated with the plastic zone may be only a few, and the effect of the grain boundary is considered to be relatively small. On the other hand, the data of H_v includes a significant effect of grain boundaries with the indent size around 50 μm (4.9 N load), which is much larger than the grain size.
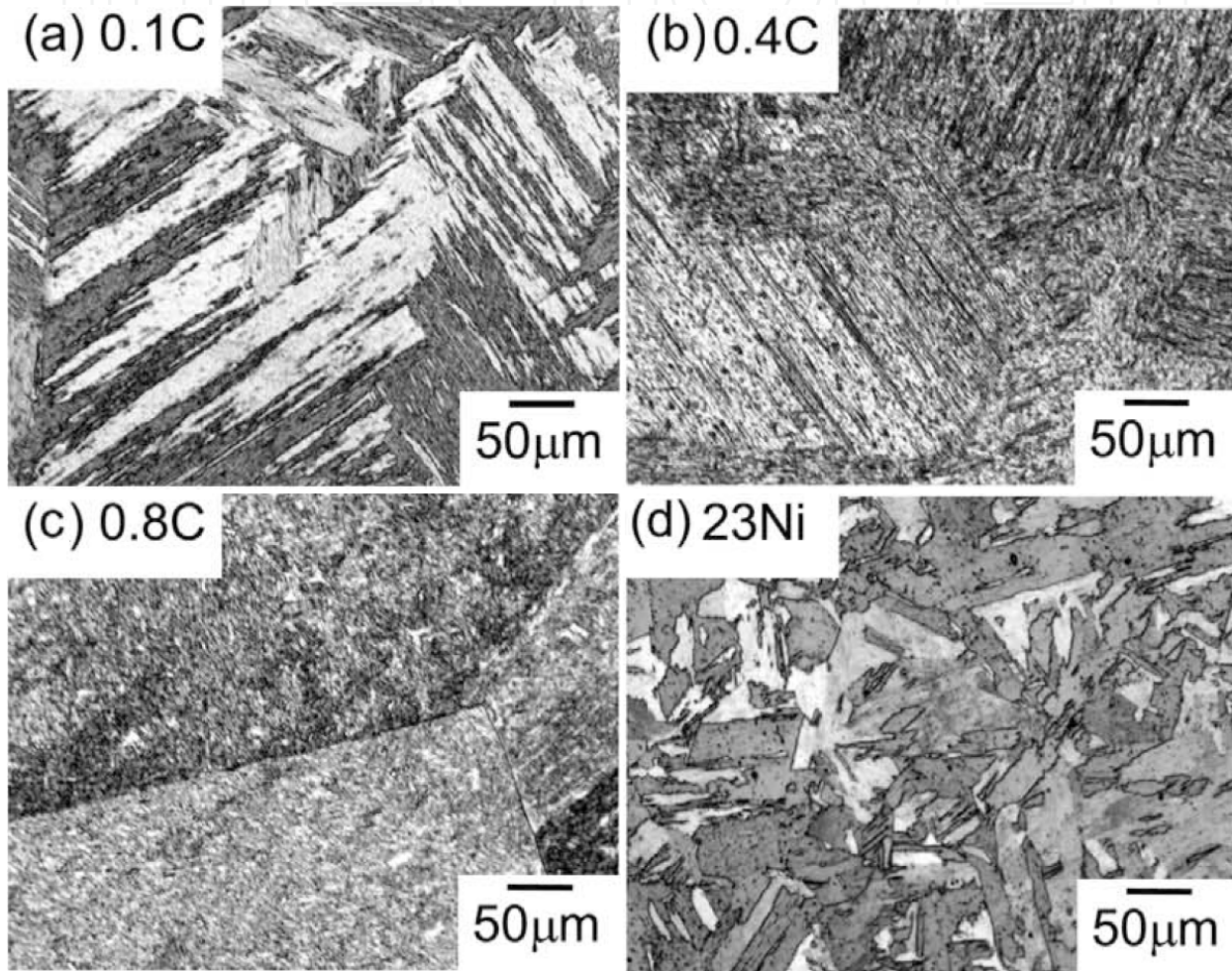

Figure 2. Optical micrographs of the Fe-C lath martensite of (a) 0.1, (b) 0.4, (c) 0.8C and (d) of the Fe-23Ni lath martensite. The block width decreases with an increase in the carbon content. The block width of the Fe-23Ni alloy is much larger than that of the Fe-C alloys.

Both nanohardness H_n and micro Vickers hardness H_v for each specimen are plotted as a function of the carbon content in Fig. 4. The standard deviation of the hardness was plotted as the error bars (an average of more than 20 data with H_n and 5 data with H_v). The hardness obviously increases with increasing carbon content, especially when it is lower than 0.6 wt%. The effect of crystallographic orientation on both the micro Vickers hardness and the nanohardness is thought to be small since the measured hardness value is close when randomly indented at various sites.
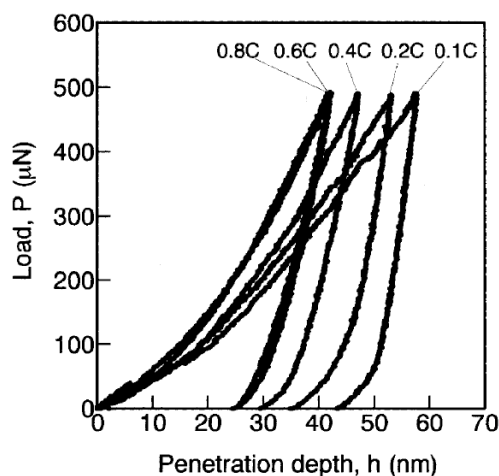
Figure 3. Typical load-displacement curves of five Fe-C martensites. The corresponding carbon content is shown in the figure.
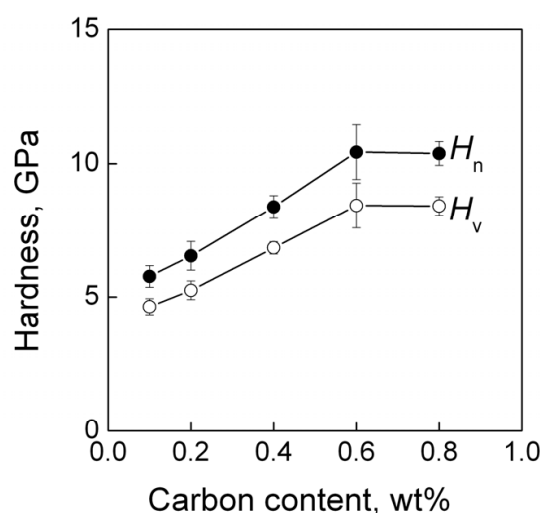

Figure 4. Nanohardness and micro Vickers hardness of the Fe-C martensite plotted as a function of carbon content.

Fig. 5 shows the relationship between the nanohardness H_n and the micro-Vickers hardness H_v for the body-centered-cubic (bcc) single crystals and the Fe–C martensite. For the single crystals that are shown by the open circles, the nanohardness is almost directly proportional to the micro-Vickers hardness. On the other hand, the series of Fe–C specimens shown by the circles are not related to the single crystal. For example, the nanohardness of 0.1C martensite is comparable to that of Mo single crystal, but the Vickers hardness of 0.1C martensite is much higher than that of Mo single crystal. The other Fe-C martensite is similar to that of 0.1C martensite. This trend suggests that the macroscopic strength in the Fe-C martensite is dominated not only by the matrix strength but by other factors on a larger scale such as the high-angle grain boundaries. The data for the Fe-23Ni martensite deviates slightly from those of the single crystals. This means that although the Fe-23Ni has a grain size effect, the contribution of grain boundaries is not very large because the block size is not as small as that of the Fe-C martensite.

The ratio H_n/H_v is used for further consideration of the contributions of the matrix strength to the macroscopic strength. This behavior of grain size effect is express in the Hall-Petch relation as [2]:
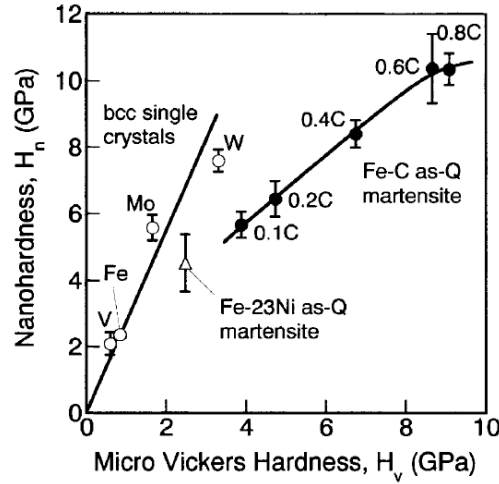
$$\frac{H_n}{H_v} = 1 - \frac{k'd^{-1/2}}{H_v}$$

(2)

Figure 5. Relationship between nanohardness H_n and micro-Vickers hardness H_v for the bcc single crystals, the Fe–C martensite and the Fe-23Ni lath martensite with a block width of a few 10μm.
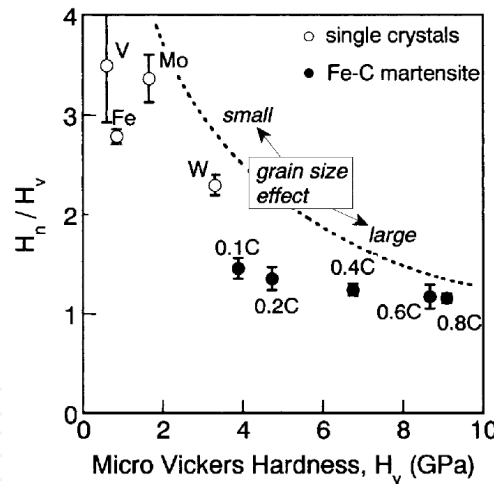

Figure 6. Relationship between micro-Vickers hardness H_v and H_n/H_v for the bcc single crystals and the Fe–C martensite.

When the locking parameter k' is constant and the grain size d approaches zero i.e. the grain size effect is large, the term $k'd^{-1/2}$ is replaced by H_v because $k'd^{-1/2}$ is much larger than H_n in Eq. 2. Accordingly, the ratio H_n/H_v approaches zero. Meanwhile, when d approaches infinity i.e. the grain size effect is small, the term $k'd^{-1/2}$ is zero, and H_v approaches H_n. This result is qualitatively represented by the broken line in Fig. 6. Note that the ration H_n/H_v does not approach 1 because the nanohardness and the Vickers hardness do not coincide due to the difference of indenter geometry and so on. Fig. 6 shows the ratio H_n/H_v for all the specimens

plotted as a function of H_v. The much lower ratio for the Fe–C martensite than those for the single crystals suggest that the contribution of the high-angle grain boundaries is large. The ratio H_n/H_v decreases with increasing carbon content, indicating that the grain-boundary effect increases with carbon content, especially for the carbon content range below 0.6 wt%.

3.3. In situ nanoindentation in transmission electron microscope (TEM) with Fe-0.4C tempered martensitic steel

Much deeper investigation was performed in Fe–0.4C tempered martensitic steel through in situ nanoindentation in TEM to study the dislocation–interface interactions in the Fe–C tempered martensitic steel. Two types of boundaries were imaged in the dislocated martensitic structure: a low-angle lath boundary and a coherent, high-angle block boundary.
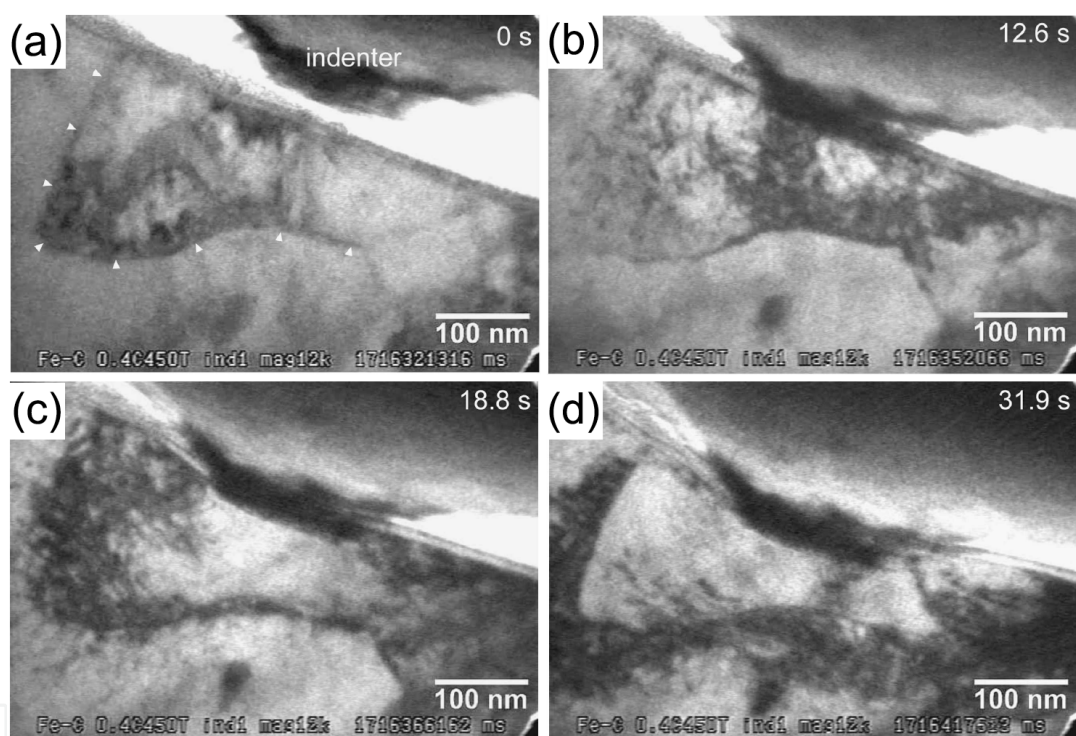

Figure 7. In situ TEM micrographs of the Fe–0.4C martensite, including a low-angle grain boundary: (a) before indentation, (b) at 21 nm penetration depth, showing dislocation emission beneath the indenter, (c) at 46 nm penetration depth, showing dislocation pile-up at the grain boundary, and (d) at 84 nm penetration depth, demonstrating dislocation emission on the far side of the grain boundary.

3.3.1. At low-angle grain boundary

Fig. 7 includes a series of video frames from the in situ TEM nanoindentation of the low-angle grain boundary. The grains on either side of the boundary have the same [111] $_{\alpha'}$ zone axis and the boundary is identified as a lath boundary. Fig. 7(a) shows the diamond indenter prior to indentation, as it approached the surface from the upper-right corner of the figure. The grain boundary is indicated by arrow-heads. As the indenter penetrated into the grain, Fig. 7(b), the deformation was accommodated by the motion of dislocations away from the

indenter contact point toward the grain boundary. The low-angle boundary offered some resistance to the dislocation motion, resulting in a pileup at the grain boundary, shown in Fig. 7(c) (a frame taken at an indenter penetration depth of 46 nm). As the indenter penetrated further, a large number of dislocations were emitted on the far side from the indenter tip (left and lower side on the micrograph) of the grain boundary into the adjacent grain. A dense and tangled dislocation structure is seen on the far side of the grain boundary in Fig. 7(d), which was taken at an 84 nm penetration depth. When the indenter was withdrawn, a high density of dislocations was retained near the far side of the boundary.

3.3.2. At high-angle grain boundary (block boundary)

The dislocation interactions with the high-angle grain boundary (block boundary) were dramatically different, as documented in Fig. 8. The misorientation across the grain boundary was determined to be about 56°, with a rotation axis near [0.16, 0.64, 0.76]. Figure 8(a) shows the initial state before indentation, with the high-angle grain boundary indicated by arrow-heads. During the early stages of the indentation dislocations can be seen to sweep across the grain from right to left, shown part-way in Fig. 8(b). Note that the pre-existing dislocations in the left area of the indented grain are not seen in the Fig. 8(b) any more, while they are clearly shown in the Fig. 8(a). This could be due to a change of diffraction condition into an invisible condition of the dislocations because of the deformation of the sample. At approximately 60 nm penetration depth, a dense cloud of dislocations reached the high-angle boundary.
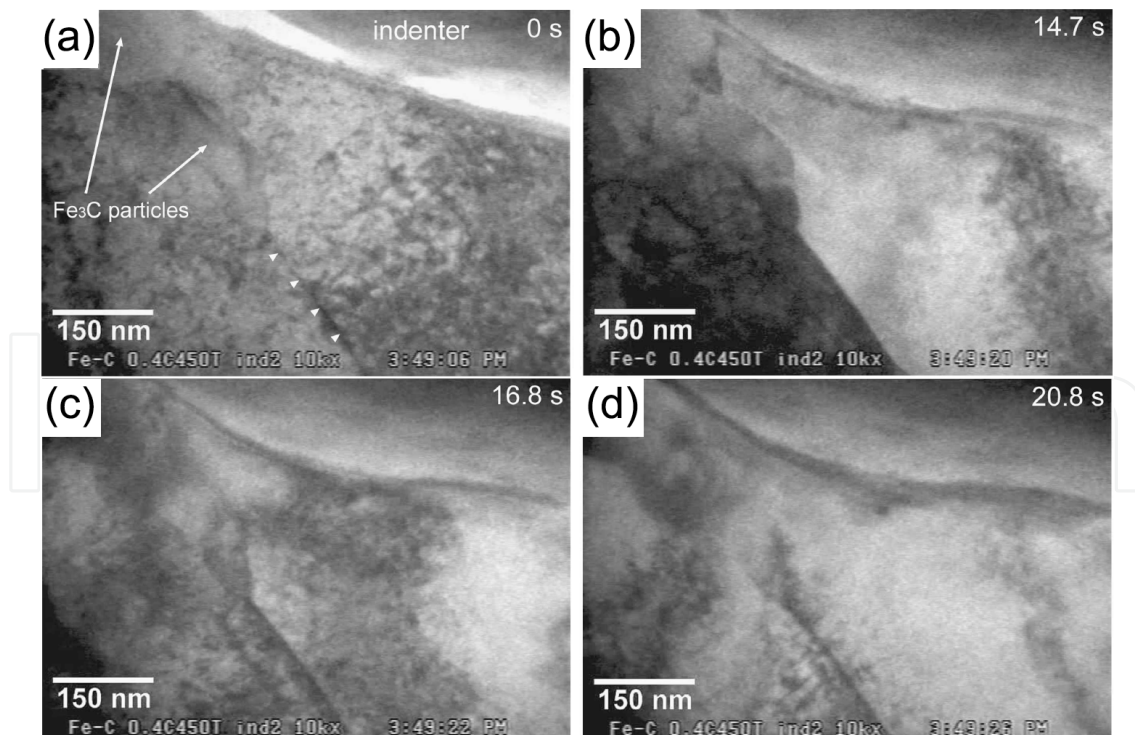

Figure 8. In situ TEM micrographs of the Fe–0.4C martensite, including a high-angle grain boundary: (a) before indentation, (b) at 70 nm penetration depth, showing dislocations sweeping across the grain from right to left, (c) at 83 nm penetration depth, showing disappearance of dislocation at the grain boundary, and (d) at 92 nm penetration depth, demonstrating no dislocation emission on the grain boundary.

However, as shown in Fig. 8(c), on reaching the boundary, the dislocations simply disappeared; there is no indication of a pileup or significant penetration into the adjacent grain. In fact, as illustrated in Fig. 8(d), there is virtually no change in the dislocation configuration on the far side of the boundary. The grain beyond the boundary is essentially unaffected. The behavior of the dislocation "sink" at the high angle grain boundary is illustrated in more detail in Fig. 9, which presents a sequence of images recorded between those in Figs. 8(c) and 8(d). The earliest image, Fig. 9(a), shows a high density of dislocations on both sides of the grain boundary. Many of the dislocations on the right side of the grain boundary are moving from right to left in the indented grain as illustrated in Fig. 8.

The video frames shown in Figs. 9(b)-(d) correspond to increasing penetration depth. As can be seen in these three frames, the dislocations on the right side of the grain boundary vanished at the boundary, while the dislocations on the left side of the grain boundary were essentially unchanged in number, density, or position during the deformation. The stable contrast in these images show that the diffraction condition in the vicinity of the grain boundary was the same throughout the deformation sequence shown, so the behavior observed was not a result of bending in the foil. This sequence demonstrates that the dislocations that approached the boundary were almost completely absorbed by it.
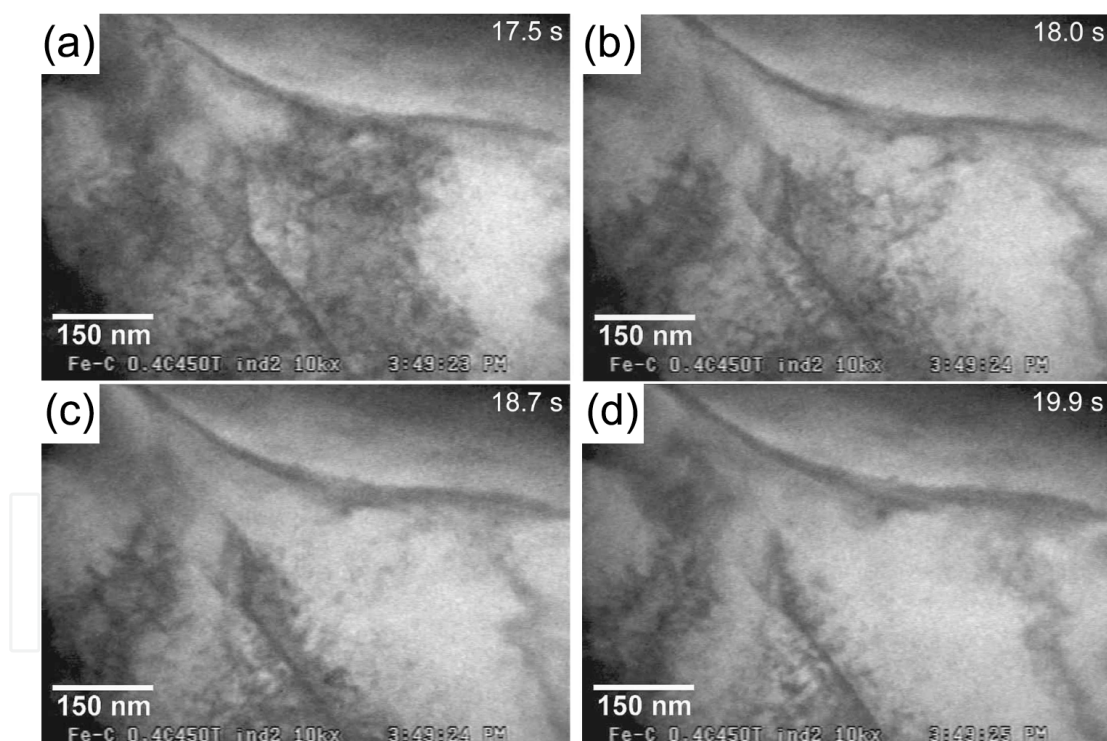

Figure 9. In situ TEM micrographs of the Fe–0.4C martensite showing details of the "sink" of dislocations at the high-angle grain boundary. Frames (a–d) correspond to a sequence between Figs. 8(c) and 8(d). Penetration depth increases from (a) to (d).

3.4. Conclusions

High purity Fe-C as-quenched martensitic steels, four bcc single crystals and an Fe-23Ni lath martensitic steel were investigated using the nanoindentation technique. In the penetration

depth range shallower than 60 nm, the indent size is a few times larger than the lath width and smaller than the block size, hence the nanohardness in this scale corresponds to the block matrix strength. The ratio of the nanohardness to the micro Vickers hardness (H_n/H_v) is much smaller for the Fe-C martensite than those of the single crystals, indicating a significant effect of grain size on the macro strength of the Fe-C martensite.

Dislocation–interface interactions in Fe–0.4C tempered martensitic steel were studied through in situ nanoindentation in a TEM. Two types of boundaries were imaged in the dislocated martensitic structure: a low-angle (probable) lath boundary and a coherent, high-angle (probable) block boundary. In the case of a low-angle grain boundary, the dislocations induced by the indenter piled up against the boundary. As the indenter penetrated further, a critical stress appeared to have been reached, and a high density of dislocations was suddenly emitted on the far side of the grain boundary into the adjacent grain. In the case of the high-angle grain boundary, the numerous dislocations that were produced by the indentation were simply absorbed into the boundary, with no indication of pileup or the transmission of strain. This surprising observation is associated with the basis of the crystallography of the block boundary [3].

3.5. Some other related researches

The temper softening behavior of Fe–C binary martensite with various carbon contents [24, 26] was also considered by evaluating the matrix strength through nanoindentation. The tempering temperature dependence of conventional micro-Vickers hardness shows a ''hump'' around 673 K, while the matrix strength obtained by nanoindentation simply decreases with tempering temperature. This is connected with the microstructure change as discussed in detail in Ref.[27]. Furthermore, the mechanical characterizations using nanoindentation technique were performed for the martensitic steel used as practical dies steel [28] containing carbide-former elements of Cr, Mo, W, and V, which are responsible for secondary hardening by tempering. The nanohardness corresponding to the matrix strength shows obvious secondary hardening, and the hardening-peak temperature coincides with that of the macroscale hardness. The results suggest that the secondary hardening of the dies steel during tempering is attributed not only to the nanoscale strengthening factors such as precipitation hardening by the alloy carbides, but also to some other factors in larger scale. One of the strengthening factors is a decomposition of retained austenite to much harder phases, such as martensite and/or ferrite–cementite constituent.

4. Nanoindentation on Fe-Ni lenticular martensite

4.1. Microstructures of Fe-Ni lenticular martensite

A Fe-33 wt% Ni alloy (shorted for Fe-33Ni) was used in the study. The full austenite phase sample used for comparison is named as RT-austenite sample 'A0'. Transformed lenticular martensite with a straight martensite/austenite (M/A) interface formed by cooling austenite sample 'A0'' in liquid nitrogen (77K) is referred to as sample 'M1', which contains the transformed lenticular martensite phase and the retained austenite phase. The substructures of

the lenticular martensite are shown by TEM micrographs from Fig. 10(a) ~ (d). As shown in Fig. 10(a), the midrib region is completely twinned with a twinning system of $(112)[111]_M$. In the twinned region (Fig. 10(b)), a small amount of transformation twins exist concurrently with a set of screw dislocations. The Burgers vector ($\vec{b} = a/2[111]_M$) is parallel to the twinning shear direction as indicated by the arrow. The structure in the untwinned region contains several sets of screw dislocations near the twinned region or the curved and tangled dislocations (marked by the circles in Fig. 10(c)) in addition to the straight dislocations (marked by the dashed lines in Fig. 10(c)) near the M/A interface. As shown in Fig. 10(d), the surrounding austenite phase close to the M/A interface also contains a high density of tangled dislocations. These dislocations are probably introduced into the austenite to accommodate the transformation strain and might be inherited during the growth of the lenticular martensite [15]. The dislocation density in the residual austenite decreases with increasing distance away from the M/A interface. In a word, the substructure of the lenticular martensite gradually transited from fully twinned in the midrib to dislocation structure in the untwinned region.
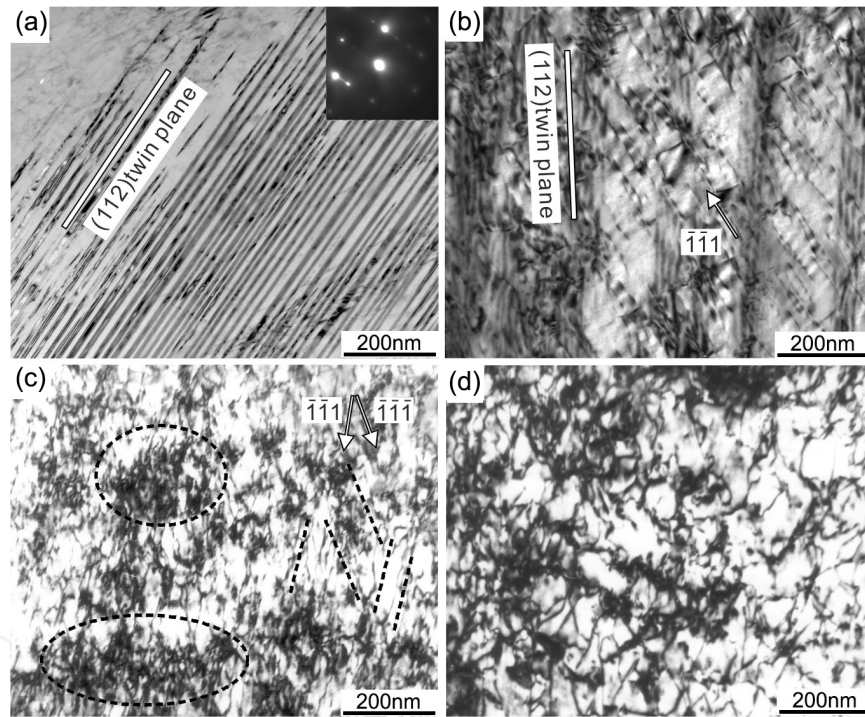

Figure 10. TEM micrographs of the substructure in the lenticular martensite, (a) midrib region, (b) twinned region, (c) untwinned region near the M/A interface and (d) austenite near the M/A interface.

4.2. Results and discussions

Fig. 11(a) is the AFM image after the nanoindentation test. The midrib in the center and the surrounding twinned region of the lenticular martensite plate can be recognized easily by the dark color. The average nanohardness values of Fe-33Ni sample M1, RT-austenite sample A0 and the Fe-23Ni sample are shown in Fig. 11(b). The nanohardness value of the midrib region, 5.22 ± 0.19 GPa, is higher than that of the other regions in the same martensite plate. A drop in

nanohardness can be observed from the midrib in the martensite phase to the austenite phase near the M/A interface. The fine twin (the midrib region) shows about a 20% higher resistance to deformation than the dislocated regions (untwined region) in the lenticular martensite (Fe-33Ni alloy) or the lath martensite (Fe-23Ni alloy). It is speculated that the dislocation motion was blocked by the twin boundaries and thus led to strengthening. However, this higher strength in the midrib region cannot be revealed by the conventional micro-Vickers hardness test since the contribution of the fine twinned region to the strength in the lenticular martensite is limited by its small volume fraction. The lath martensite of the Fe-23Ni alloy (dislocated) has an average nanohardness value smaller than that of the midrib region (fully twinned) and larger than that of the untwinned region (dislocated) in the Fe-33Ni lenticular martensite sample M1. The difference in chemical compositions of both alloys might affect their hardness as well, but the influence should be small compared with the difference in the substructure [7, 29]. For both dislocated substructures, the lath martensite had higher dislocation densities (8.5 ~ 12.4 ×10^{14} m^{-2}) in the Fe-23Ni alloy [8] than that of the untwined region (4.7 ~ 9.1 ×10^{14} m^{-2}) in the Fe-33Ni [30] lenticular martensite. The nanohardness of the austenite phase near the M/A interface is slightly higher than that of the austenite far from the M/A interface. The dislocation density decreases as the distance from the M/A interface increases and causes a decrease in the nanohardness of the austenite phase.
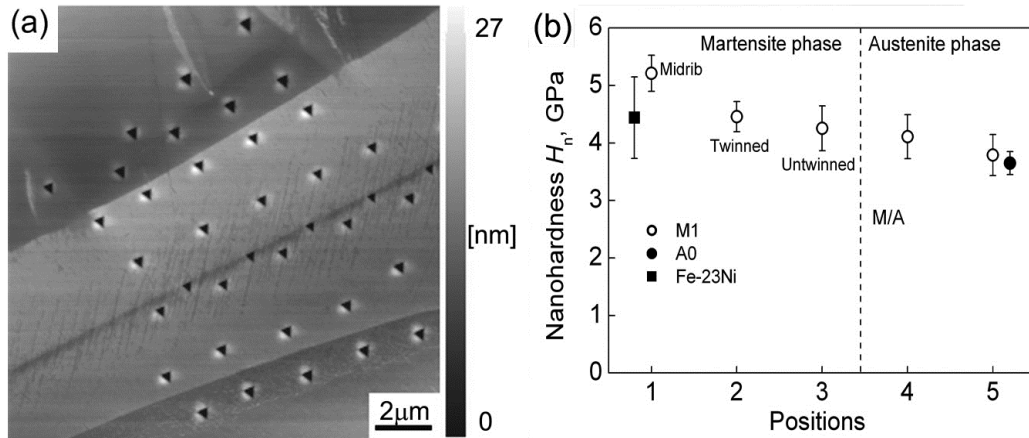

Figure 11. (a) the AFM image after the nanoindentation test and (b) nanohardness values of the transformed martensite sample M1 at various positions, RT-austenite sample A0, and the lath martensite of a Fe-23Ni alloy.
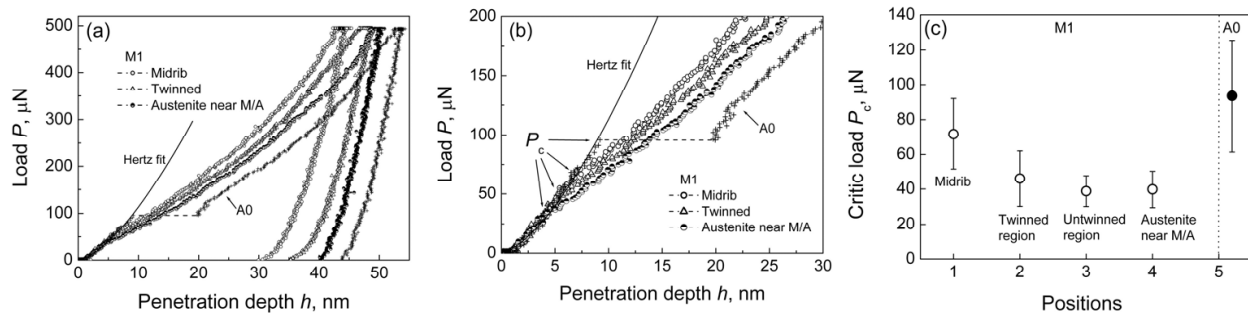

Figure 12. Typical load–depth curves of the transformed martensite sample M1 and RT-austenite sample A0 (a) and a magnified view under ultra-low loads (b); (c) is the average critical load in the various substructures.

The typical load-depth curves of the lenticular martensite sample M1 and RT-austenite sample A0 are shown in Fig. 12(a). According to the earlier reports, the initial stage of loading is of a purely elastic nature and can be described by the Hertz contact theory [31, 32]:

$$P = \frac{4}{3} E_r R^{1/2} h^{3/2},$$ (3)

where P is the applied load, R is the indenter tip radius, h is the displacement/depth, and E_r is the reduced modulus. As shown in Fig. 12(a), the initial portion of the load-depth curve fits the Hertz contact theory well by putting the values of the reduced modulus E_r (173±18 GPa) and the tip radius ($R = 200$ nm) into the equation (3). When the applied load is higher than about 40 µN, the curves begin to deviate from the Hertz fit, which marks the onset of plastic deformation.

Fig. 12(b) is a magnified view of Fig. 12(a) in the load range below 200 µN, showing the initial stage of the indentation-induced deformation. The load-depth curves of the RT-austenite sample A0 shows a strain burst in the loading curve, which is called a pop-in event. The load where the pop-in event sets in is defined as a critical load P_c. The pop-in behavior has been reported to be associated with a nucleation and propagation of dislocations under an initial elastic strain field or a defect-free region in the metals [24, 33-35]. The obvious pop-in behavior in the sample A0 is consistent with the property where the untransformed RT-austenite phase has a lower dislocation density than that of the transformed martensite phase. The critical stress of the pop-in event can be estimated as 7.3 GPa through the Hertz contact theory where the maximum shear stress τ_{max} [36] beneath the indenter can be given as:

$$\tau_{max} = 0.18 \cdot \left(\frac{E_r}{R} \right)^{\frac{2}{3}} P^{\frac{1}{3}},$$ (4)

which is in an order of an ideal strength. For the transformed martensite sample M1 which contains a high density of defects (twins or dislocations), the load-depth curves do not show a pop-in event but undergo an apparent slope change which marks the onset of plastic deformation. The changing point of the load is also defined as critical load P_c for easy comparison, as indicated by the arrows in Fig. 12(b). The average P_c at different regions of the samples M1 and A0 are shown in Fig. 12(c). In the transformed martensite sample M1, the critical load of the midrib region is higher than that of the other regions but lower than that of the RT-austenite sample A0.

Note that the strain rates vary when the plasticity initiation occurs. A classic model based on the dislocation theory expresses a strain rate $\dot{\gamma}$ as

$$\dot{\gamma} = \rho \cdot b \cdot \bar{v},$$ (5)

where ρ is the mobile dislocation density, b is the magnitude of the Burgers vector and $\bar{v}$ is the average dislocation velocity. The difference in the critical load and the strain rate is associated with the different plastic deformation behaviors in the various substructures and will be discussed by the interaction between the pre-existing lattice defects (twin or

dislocation structure) and the newly formed dislocations during the indentation process. In the RT-austenite sample A0, the density of pre-existing dislocations is very low, thus the probability of a mobile dislocation existing underneath the indenter is also significantly low. Therefore, the stress required for the nucleation of dislocations in the defect free region is high, which is close to the ideal strength and results in the highest critical load P_c as shown in Fig. 12(c). After the initiation of plastic deformation, the strain rate in the RT-austenite phase is quite high; this is understood by the remarkable strain burst as the obvious pop-in event. Once the plastic deformation is initiated and a dislocation source is activated, many mobile dislocations become present in the stress field producing a high ρ value. Additionally, the $\bar{v}$ could also be high since the density of pre-existing dislocations as obstacles for the dislocation movement is significantly low. After the pop-in event, plastic deformation expands far from the initiation point and the low density of pre-existing dislocations also causes a lower flow stress in a further deformation stage resulting in a relatively low nanohardness in the RT-austenite sample A0. This result indicates that high flow stress is not necessarily obtained in a microstructure with high critical stress for plasticity initiation.

In the regions with high dislocation densities, deformation underneath the indenter could be initiated at much lower loads since the stresses required for the motion of pre-existing dislocations are much lower than the stress required for the nucleation of dislocations [37]. This is an appropriate reason for the much lower critical loads in the dislocated structure of the martensite phase in the sample M1. After the initiation of plastic deformation, moving dislocations interact with other pre-existing dislocations; hence the average dislocation velocity $\bar{v}$ is significantly low. Therefore, the strain rate $\dot{\gamma}$ is also very low and a higher applied stress is necessary for further deformation. This does not result in a pop-in behavior, causing only a change in the slope of loading curve, and inevitably leads to higher nanohardness in the dislocated regions than that of the RT-austenite sample A0.

In the midrib region, the existing twins may act as a stress concentrated site at the subsurface for the nucleation of dislocations, even though there are only a few pre-existing dislocations, and produce a relatively lower critical load than that of the defect-free RT-austenite sample A0. On the other hand, the twin structure could act as an obstacle to the dislocation motion like that of the pre-existing dislocations, and lead to the same deformation behavior as that of the dislocated regions. Furthermore, the very fine twin structure in the midrib region causes a much higher flow stress and higher nanohardness than that of any other regions and phases. The mixed structure of twin and dislocation in the twinned region has a critical load P_c between the midrib and untwinned region.

4.3. Conclusions

Nanoindentation tests were conducted on the lenticular martensite of a Fe–33Ni alloy to reveal the deformation behavior of each component with different lattice defects. A continuous drop in nanohardness from the midrib in the martensite phase to the austenite phase was observed in the transformed martensite sample M1. The nanohardness value of the midrib region was about 20% higher than that of the other regions; however, its

contribution to the macroscopic strength was small due to its limited volume fraction. Plasticity initiation and subsequent deformation behavior depended on the microstructures. In the RT-austenite sample A0, the low density of pre-existing dislocation caused a high critical load of plasticity initiation and a low flow stress. In contrast, plasticity initiation occurred rather easily in highly dislocated regions such as the untwinned region and the austenite phase near the M/A interface in the sample M1; however, the subsequent flow stresses were higher than that of the defect-free RT-austenite sample A0. The very fine twin structure in the midrib region in the sample M1 had two roles: one was to assist the plasticity initiation as a stress concentrated site and the other was to act as a strong obstacle to the dislocation motions.

5. Nanoindentation test on surface mechanical attrition treated NiTi shape memory alloy

5.1. Results and discussions

The NiTi samples were subjected to SMAT at room temperature using bearing steel balls with a diameter of 5 mm for 5 and 60 min (hereafter denoted SMAT-5 and SMAT-60, respectively). NiTi samples before SMAT contained a coarse grained austenite (B2) phase at room temperature. After SMAT near equiaxial B2 nanograins were produced on the surface. Variations in grain size (d) with respect to the distance from the SMAT surface (D) for the SMAT-5 and SMAT-60 samples are shown in Fig. 13(a). For both samples grain size d decreased gradually with decreasing distance D, whereas the SMAT-5 sample had a larger d at the same D. Fig. 13(b) shows typical force-indentation depth curves at different D for SMAT-60. Significant differences in those curves are clearly visible.
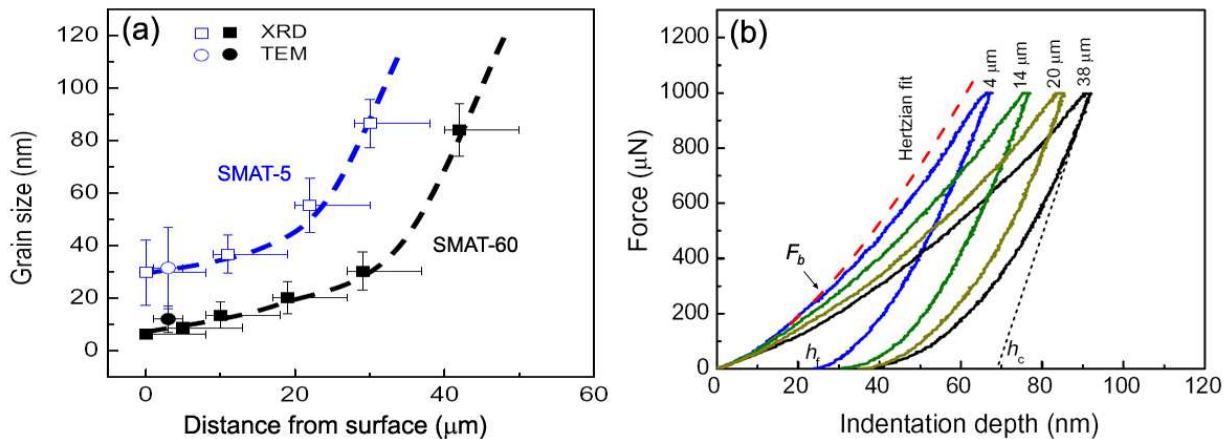

Figure 13. (a) Variation in grain size with distance from the surface for SMAT samples. (b) Typical force–indentation depth curves at different distance D for SMAT-60 as indicated. Definition of the bifurcating force F_b, h_c and h_f are indicated.

Fig. 14(a) demonstrates the determined values of Young's moduli E as a function of D for a large number of measurements in different regions of the two samples. For the SMAT-60 sample a remarkable increase in E with decreasing D was obtained. E increased from about 60 GPa at 40 μm to 85 GPa at 2 μm distance. For the SMAT-5 sample the increase in E was

less remarkable. *E* increased from about 60 GPa at 30 μm to about 70 GPa at 2 μm distance. Using the measured grain size, *E* was plotted against *d* for the two samples, as shown in Fig. 14(b). An obvious dependence of *E* on *d* can be seen in Fig. 14(b). *E* increased dramatically with decreasing *d* for *d* less than 100 nm. For comparison, the Young's modulus of amorphous NiTi was also measured and is in agreement with the reported value (~93 GPa) [38]. The Young's modulus of NiTi, as measured by the rectangular parallelepiped resonance (RPR) method [39], is also included in Fig. 14(b). The maximum Young's modulus obtained for the present NiTi sample (~85 GPa for *d* ~ 6 nm) is close to that measured by RPR and that of amorphous NiTi, and is higher than that of partially amorphous NiTi (71 GPa) [40].
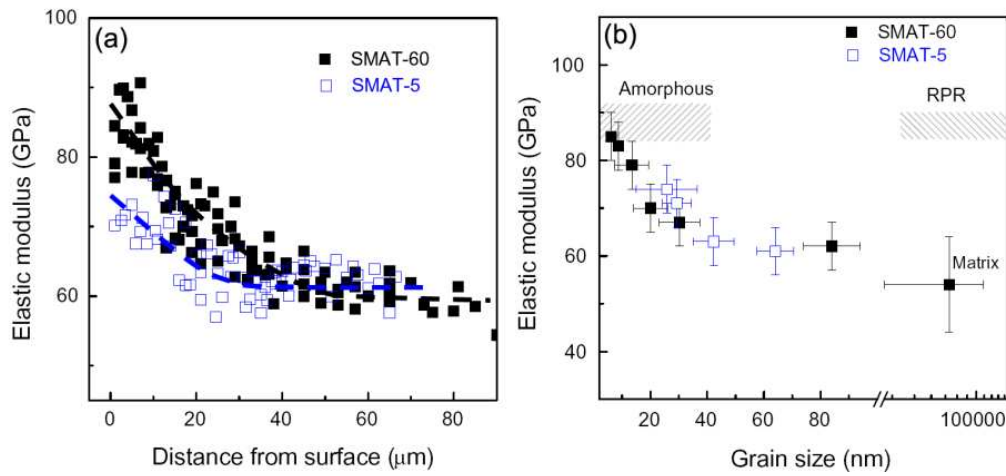

Figure 14. (a) Calculated Young's modulus as a function of distance from the surface. Dashed lines are guides for the eye. (b) Calculated Young's modulus as a function of grain size. The Young's moduli of NiTi determined by the RPR method and that of amorphous NiTi are also indicated.
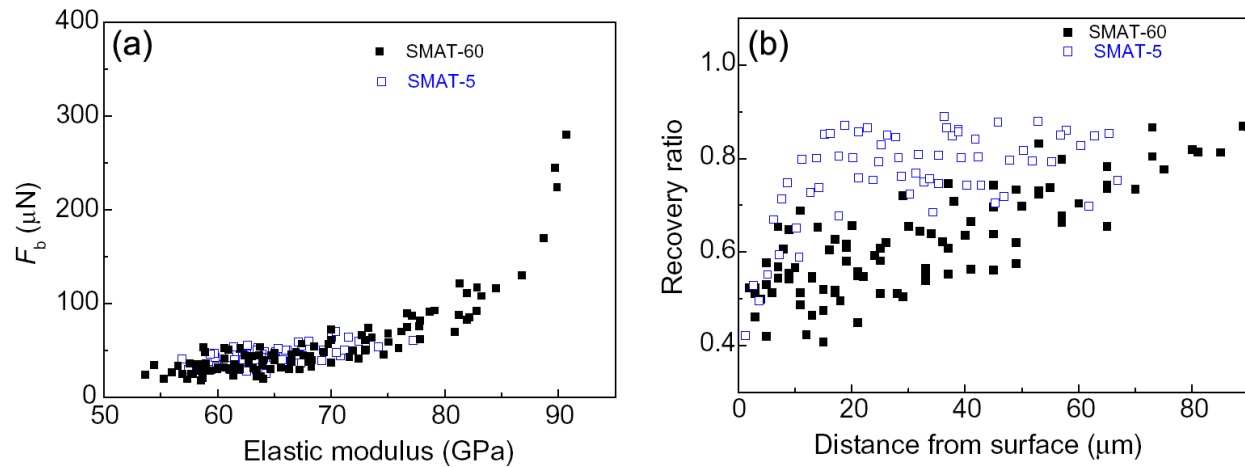

Figure 15. (a) Relationship between the bifurcating force (F_b) and Young's modulus. (b) Indentation recovery ratio as a function of distance from the surface.

The remarkable dependence of *E* on *d* was somewhat unexpected, because grain size has usually been believed to have little effect on the Young's modulus of nanocrystalline materials. It should be noted that residual stress may have an effect on the Young's modulus, typically a change of <1% for a compressive stress of 100 MPa [41], which is,

however, rather small compared with the large enhancement of Young's modulus (~40%) in the present study. Moreover, it was found that the compressive stress in SMAT samples increased with increasing D, with a maximum in the subsurface instead of the top surface [42]. Obviously, the effect of residual stress can be excluded. Actually, no change in Young's modulus has ever been reported in previous SMAT samples [43]. Therefore, the observed dependence of E on d should be related to the unique properties of NiTi. It is speculated that the transformation stress for the SIM increases with decreasing grain size for nanograins. Thus, the measured dependence of E on d is related to the grain size effect on the SIM in nanocrystalline NiTi, i.e. suppression of the SIM leads to the increase in E with decreasing d.

As indicated in Fig. 13, the bifurcating force (F_b) is defined as the point where the indentation loading curve starts to deviate from the purely elastic curve determined by Hertz contact theory. The bifurcating force is related to the transformation stress, i.e. a higher transformation stress leads to a higher bifurcating force, and vice versa. As shown in Fig. 15(a), a higher Young's modulus corresponds to a higher bifurcating force and, hence, a higher transformation stress. This clearly indicates that the increase in Young's modulus is related to suppression of the SIM with the reduction of grain size. Indentation depth recovery is also a strong indication of the SIM effect. The recovery ratio (δ) was introduced as a measure of the recovery due to the SIM and is defined as [44]:

$$\delta = \frac{h_c - h_f}{h_c},\tag{6}$$

Definitions of h_c and h_f are indicated in Fig. 13(b). Suppression of the SIM can be demonstrated quantitatively by plotting δ against D. As shown in Fig. 15(b), δ decreased with decreasing D, indicating less recovery due to less SIM for smaller D and d. Thus, the measured dependence of E on d is related to the grain size effect on the SIM in nanocrystalline NiTi, i.e. suppression of the SIM leads to the increase in E with decreasing d. The highest value of E for a d of ~6 nm was close to the intrinsic value of crystalline and amorphous NiTi, although, as indicated in Fig. 14(b), the SIM may not be completely suppressed for a d of ~6 nm. By further extrapolation of the E–d relationship to a d of 0 nm, a value of E equal to 90 GPa is derived, which can be considered the intrinsic value for NiTi by complete suppression of the SIM in this study. This value was used for Hertz fitting in Fig. 13, and a good fit of the initial part of the loading curve was obtained.

5.2. Conclusions

In summary, a nanocrystalline surface layer with a graded grain size distribution was produced on NiTi by SMAT. The apparent Young's modulus, as measured by nanoindentation, was found to increase dramatically with decreasing D and d, and reached ~85 GPa for d ~ 6 nm. Such dependence of E on d can be attributed to the suppression of the SIM in nanocrystalline NiTi. The present study has provided unambiguous experimental evidence indicating that the Young's modulus of NiTi can be underestimated due to the SIM, and by suppression of SIM in nanocrystalline NiTi an enhanced Young's modulus can be obtained, approaching the intrinsic value for NiTi.

5.3. Some other related researches

Furthermore, nanoindentation was conducted in a Fe–28Mn–6Si–5Cr alloy [45] to investigate the stress-induced ε-martensitic transformation behavior and the shape memory effect. The shape memory effect of Fe–Mn-based alloys is derived from the stress-induced ε-martensitic transformation (face-centered cubic (fcc) to hexagonal close packed (hcp)) [46]. Since the pre-strains required for shape memory are 2–6% [47], an understanding of the initial deformation behavior, including the ε-martensitic transformation, is extremely important for any investigation of the shape memory effect. The ε-martensitic transformation has a number of distinctive characteristics, including low critical stress [48], remarkable crystallographic orientation dependence [49], specific surface relief, and reversibility. However, the analyses essential for determining the characteristics of shape memory alloys (SMAs) are difficult due to the existence of grain boundaries, twin boundaries and thermally induced ε-martensite. A nanoindentation test is useful for investigating the initial deformation behavior since the test can be performed on several positions over a limited area and enables the load–displacement behavior of the entire process to be observed. The indentation of austenite has been reported to create high stresses under diamond indenters that can cause stress-induced martensitic transformation in Fe–0.08C–0.5Si–1Al–7Mn (wt.%) [50]. Additionally, the combination of nanoindentation with AFM makes it possible to observe indentation-induced surface relief in the CuAlNi SMA [51] and to evaluate shape memory effects in the NiTi SMA [52]. Hence, the nanoindentation test appears to be suitable for evaluating the ε-martensitic transformation behavior in a specific orientation of a bulk material based on a careful study of the above-mentioned characteristics of the ε-martensitic transformation. Nanoindentation tests and AFM observations were performed in a Fe–28Mn–6Si–5Cr alloy [45] to investigate the stress-induced ε-martensitic transformation behavior and the shape memory effect. The shape memory effect was evaluated from the volume change in an indent mark caused by annealing measured by atomic force microscopy. Using the load–displacement (P–h) data obtained from nanoindentation, the plot of P/h vs. h showed two types of slopes, corresponding to the ε-martensitic transformation and slip deformation, and exhibited a correlation with the shape recovery ratio.

6. Chapter summary

As mentioned above, nanoindentation technique has been used in martensitic structures to fulfill various missions. Such as nanohardness test and Young's modulus measurement which can measure the mechanical properties of a precise site in a microstructure with accuracy within a nanometer. But its capability is not limited to this simple usage. By correlating the microstructure change with the load-depth curve, the underlying mechanism can be revealed. And it is definitely will be used more widely in the future.

Author details

L. Zhang and T. Ohmura
National Institute for Materials Science, 1-2-1 Sengen, Tsukuba, Ibaraki, Japan

K. Tsuzaki

National Institute for Materials Science, 1-2-1 Sengen, Tsukuba, Ibaraki, Japan
Graduate School of Pure and Applied Sciences, University of Tsukuba, Ibaraki, Japan

7. References

[1] A. Gouldstone, N. Chollacoop, M. Dao, J. Li, A. M. Minor, Y.-L. Shen, Indentation across size scales and displines: Recent developments in experimentation and modeling. Acta Mater. 55 (2007) 4015-4039.

[2] T. Ohmura, K. Tsuzaki, S. Matsuoka, Nanohardness measurement of high-purity Fe-C martensite. Scripta Mater. 45 (2001) 889-894.

[3] T. Ohmura, A. M. Minor, E. A. Stach, J. W. Morris Jr., Dislocation–grain boundary interactions in martensitic steel observed through in situ nanoindentation in a transmission electron microscope. J. Mater. Res. 19 (2004) 3626-3632.

[4] L. Zhang, T. Ohmura, A. Shibata, K. Tsuzaki, Characterization of local deformation behavior of Fe-Ni lenticular martensite by nanoindentation. Mater. Sci. Eng. A527 (2010) 1869-1874.

[5] Q. S. Mei, L. Zhang, K. Tsuchiya, H. Gao, T. Ohmura, K. Tsuzaki, Grain size dependence of the elastic modulus in nanostructured NiTi. Scripta Mater. 63 (2010) 977-980.

[6] T. Maki, Microstructure and mechanical behaviour of ferrous martensite. Mater. Sci. Forum 56-58 (1990) 157-168.

[7] M. J. Roberts, W. S. Owen, The strength of martensitic iron-nickel alloys. Trans. ASM 60 (1967) 687-692.

[8] S. Morito, J. Nishikawa, T. Maki, Dislocation density within lath martensite in Fe-C and Fe-Ni alloys. ISIJ Int. 43 (2003) 1475-1477.

[9] A. R. Marder, G.Krauss, The morphology of martensite in iron-carbon alloys. Trans ASM 60 (1967) 651-660.

[10] A. R. Marder, G. Krauss, The Formation of Low-Carbon Martensite in Fe-C Alloys. Trans ASM 62 (1969) 957-964.

[11] J. M. Marder, A. R. Marder, The morphology of iron-nickel massive martensite. Trans ASM 62 (1969) 1-10.

[12] T. Maki, K.Tsuzaki, I. Tamura, The morphology of microstructure composed of lath martensites in steels. Trans ISIJ 20 (1980) 207.

[13] R. A. Grange, C. R. Hribal, L. F. Porter, Hardness of Tempered Martensite in Carbon and Low- Alloy Steels. Metall Trans. A 8 (1977) 1775-1785.

[14] G. R. Speich, W. C. Leslie, Tempering of Steel. Metall Trans 3 (1972) 1043-1054.

[15] A. Shibata, S. Morito, T. Furuhara, T. Maki, Local orientation change inside lenticular martensite plate in Fe–33Ni alloy. Scripta Mater. 53 (2005) 597-602.

[16] A. Shibata, T. Murakami, S. Morito, T. Furuhara, T. Maki, The origin of midrib in lenticular martensite. Mater. Trans. 49 (2008) 1242-1248.

[17] T. Kakeshita, K. Shimizu, T. Maki, I. Tamura, Growth behavior of lenticular and thin plate martensites in ferrous alloys and steels. Scripta Metall. 14 (1980) 1067-1070.

[18] M. Dechamps, L. M. Brown, Structure of twins in Fe-Ni martensite. Acta Metall. 27 (1979) 1281-1291.

[19] K. Otsuka, X. Ren, Physical metallurgy of Ti-Ni-based shape memory alloys. Prog. Mater. Sci. 50 (2005) 511-678.

[20] Y. Liu, H. Xiang, Apparent Modulus of Elasticity of Near-Equiatomic NiTi. J. Alloys Compd. 270 (1998) 154-159.

[21] C. P. Frick, A. M. Ortega, J. Tyber, K. Gall, H. J. Maier, Multiscale Structure and Properties of Cast and Deformation Processed Polycrystalline NiTi Shape-Memory Alloys. Metall. Mater. Trans. A 35 (2004) 2013-2025.

[22] L. M. Qian, X. D. Xian, Q. P. Sun, T. X. Yu, Anomalous relationship between hardness and wear properties of a superelastic nickel-titanium alloy. Appl. Phys. Lett. 84 (2004) 1076-1078.

[23] T. Waitz, T. Antretter, F. G. Fischer, N. K. Simha, H. P. Karnthaler, Size Effects on the Martensitic Phase Transformation of NiTi Nanograins. J. Mech. Phys. Solids 55 (2007) 419-444.

[24] T. Ohmura, K. Tsuzaki, S. Matsuoka, Evaluation of the matrix strength of Fe-0.4 wt% C tempered martensite using nanoindentation techniques. Philos. Mag. A 82 (2002) 1903-1910.

[25] M. Itokazu, Y. Murakami, Elastic-plastic analysis of triangular pyramidal indentation. Trans. Jpn. Soc. Mech. Eng. A59 (1993) 2560-2568.

[26] T. Ohmura, T. Hara, K. Tsuzaki., Relationship between nanohardness and microstructures in high-purity Fe-C as-quenched and quench-tempered martensite. J. Mater. Res. 18 (2003) 1465-1470.

[27] T. Ohmura, T. Hara, K. Tsuzaki, Evaluation of temper softening behavior of Fe-C binary martensitic steels by nanoindentation. Scripta Mater. 49 (2003) 1157-1162.

[28] T. Ohmura, T. Hara, K. Tsuzaki, H. Nakatsu, Y. Tamura, Mechanical characterization of secondary-hardening martensitic steel using nanoindentation. J. Mater. Res. 19 (2004) 79-84.

[29] J. M. Chilton, P. M. Kelly, The strength of ferrous martensite. Acta Metall. 16 (1968) 637-656.

[30] A. Shibata, S. Morito, T. Furuhara, T. Maki, Substructures of lenticular martensites with different martensite start temperatures in ferrous alloys. Acta Mater. 57 (2009) 483-492.

[31] B. Yang, H. Vehoff, Dependence of nanohardness upon indentation size and grain size - a local examination of the interaction between dislocations and grain boundaries. Acta Mater. 55 (2007) 849.

[32] K. Durst, B. Backes, O. Franke, M. Göken, Indentation size effect in metallic material: Modeling strength from pop-in to macroscopic hardness using geometrically necessary dislocations. Acta Mater. 54 (2006) 2547-2555.

[33] A. Gouldstone, H.-J. Koh, K.-Y. Zeng, A. E. Giannakopoulos, S. Suresh, Discrete and continuous deformation during nanoindentation of thin films. Acta Mater. 48 (2000) 2277-2295.

[34] A. M. Minor, J. W. Morris Jr., E. A. Stach, Quantitative in situ nanoindentation in an electron microscope. Appl. Phys. Lett. 79 (2001) 1625-1627.

[35] L. Zhang, T. Ohmura, K. Seikido, K. Nakajima, T. Hara, K. Tsuzaki, Direct observation of plastic deformation in iron–3% silicon single crystal by in situ nanoindentation in transmission electron microscopy. Scripta Mater. 64 (2011) 919-922.

[36] T. Ohmura, K. Tsuzaki, F. Yin, Nanoindentation-induced deformation behavior in the vicinity of single grain boundary of interstitial-free steel. Mater. Trans. 46 (2005) 2026-2029.

[37] D. Lorenz, A. Zeckzer, U. Hilpert, P. Grau, H. Johansen, H. S. Leipner, Pop-in effect as homogeneous nucleation of dislocations during nanoindentation. Phys. Rev. B 67 (2003) 172101.

[38] A. Gyobu, Y. Kawamura, T. Saburi, H. Horikawa, in: M. A. Imam, R. Denale, S. Hanada, Z. Zhong, D. N. Lee (Eds.), PRICM 3, TMS, Warrendale, PA, 1998, p. 2719.

[39] X. Ren, N. Miura, J. Zhang, K. Otsuka, K. Tanaka, M. Koiwa, A comparative study of elastic constants of Ti–Ni-based alloys prior to martensitic transformation. Mater. Sci. Eng. A 312 (2001) 196-206.

[40] K. Tsuchiya, Y. Hada, T. Koyano, K. Nakajima, M. Ohnuma, T. Koike, Y. Todaka, M. Umemoto, Production of TiNi amorphous/nanocrystalline wires with high strength and elastic modulus by severe cold drawing. Scripta Mater. 60 (2009) 749-752.

[41] T. Y. Tsui, W. C. Oliver, G. M. Pharr, Influences of stress on the measurement of mechanical properties using nanoindentation. 1. Experimental studies in an aluminum alloy. J. Mater. Res. 11 (1996) 752-759.

[42] A. L. Ortiz, J. Tian, L. L. Shaw, P. K. Liaw, Experimental study of the microstructure and stress state of shot peened and surface mechanical attrition treated nickel alloys. Scripta Mater. 62 (2010) 129-132.

[43] N. R. Tao, W. P. Tong, Z. B. Wang, W. Wang, M. L. Sui, J. Lu, K. Lu, Mechanical and wear properties of nanostructured surface layer in iron induced by surface mechanical attrition treatment. J. Mater. Sci. Tech. (2003) 563-566.

[44] W. Ni, Y.-T. Cheng, D. S. Grummon, Recovery of microindents in a nickel– titanium shape-memory alloy: a self-healing effect. Appl. Phys. Lett. 80 (2002) 3310-3312.

[45] K. Sekido, T. Ohmura, T. Sawaguchi, M. Koyama, H. W. Park, K. Tsuzaki, Nanoindentation/atomic force microscopy analyses of e-martensitic transformation and shape memory effect in Fe-28Mn-6Si-5Cr alloy. Scripta Mater. 65 (2011) 942-945.

[46] K. Enami, A. Nagasawa, S. Nenno, Reversible Shape Memory Effect in Fe-base Alloys. Scripta Metall. 9 (1975) 941-948.

[47] M. Koyama, T. Sawaguchi, K. Tsuzaki, Si content dependence on shape memory and tensile properties in Fe–Mn–Si–C alloys. Mater. Sci. Eng. A 528 (2011) 2882-2888.

[48] A. Sato, H. Kubo, T. Maruyama, Mechanical Properties of Fe-Mn-Si Based SMA and the Application. Mater. Trans. 47 (2006) 571-579.

[49] A. Sato, E. Chishima, Y. Yamaji, T. Mori, Orientation and composition dependencias of shape memory effect in Fe-Mn-Si alloys. Acta Metall. 32 (1984) 539-547.

[50] T. H. Ahn, C. S. Oh, D. H. Kim, K. H. Oh, H. Bei, E. P. George, H. N. Han, Investigation of strain-induced martensitic transformation in metastable austenite using nanoindentation. Scripta Mater. 63 (2010) 540-543.

[51] W. C. Crone, H. Brock, A. Creuziger, Nanoindentation and microindentation of CuAlNi shape memory alloy. Exp. Mech. 47 (2007) 133-142.

[52] C. P. Frick, T. W. Lang, K. Spark, K. Gall, Stress-Induced Martensitic Transformations and Shape Memory at Nanometer Scales. Acta Mater. 54 (2006) 2223-2234.